Resonant islands of effective-one-body dynamics

Che-Yu Chen,[1,*] Feng-Li Lin,[2,3,†] and Avani Patel[2,3,‡]
[1]*Institute of Physics, Academia Sinica, Taipei 11529, Taiwan*
[2]*Center of Astronomy and Gravitation, National Taiwan Normal University, Taipei 11677, Taiwan*
[3]*Department of Physics, National Taiwan Normal University, Taipei 11677, Taiwan*

(Received 7 July 2022; accepted 18 October 2022; published 31 October 2022)

We study the chaotic signatures of the geodesic dynamics of a nonspinning test particle in the effective-one-body (EOB) formalism for the inspiral process of spinning binary black holes. We first show that the second-order post-Newtonian (2PN) EOB dynamics is nonintegrable by demonstrating that the EOB metric does not satisfy the criterion for the existence of the Carter constant. We then employ the numerical study to find the plateaus of the rotation curve, which are associated with the existence of Birkhoff islands in the Poincaré surface of section, signifying the chaotic dynamics in the system. Our results show the signatures of chaos for the EOB dynamics, especially in the regime of interest for which the Kerr bounds of the component black holes hold. We also find that chaotic behavior is more obvious as the spin parameter a of the deformed EOB background metric increases. Our results can help to uncover the implications of dynamical chaos in gravitational wave astronomy. Finally, we also present some preliminary results due to corrections at 3PN order.

DOI: 10.1103/PhysRevD.106.084064

I. INTRODUCTION

The inspiral binary black holes are the most common sources of gravitational waves detected by the Laser Interferometer Gravitational Wave Observatory and Virgo [1]. To detect such signals, precise theoretical gravitational waveforms should be prepared to perform the matched filtering procedure for combating the background noise in the detector. Therefore, studying the inspiral dynamics and the subsequent merger is important to obtain the gravitational waveforms. During the inspiral phase, the post-Newtonian approximation can be adopted so that the nonlinear effects of Einstein's gravity can be taken into account perturbatively. However, strong gravity will be involved in the merger phase so that only numerical relativity can yield precise dynamics and waveforms. After the merger, the dynamics can be approximated by black hole perturbation theory to uncover the quasinormal modes in the ringdown phase. Although numerical relativity can be used as a first-principle method to calculate the dynamics and waveforms for the whole coalescence of binary black holes, it is computationally very costly. Therefore, some approximate hybrid methods have been proposed to balance efficiency and accuracy requirements. Among them, the most synergistic is the effective-one-body (EOB) method [2–6]. The basic idea of the EOB method is to map the binary inspiral post-Newtonian dynamics into the reduced dynamics of a test body moving in some blackholelike background metric. The EOB map is a generalization of the Newtonian reduction of the two-body problem. The advantage of this reduction is to give the leverage to extrapolate to merger dynamics provided by numerical relativity, and then connect to the ringdown phase which is by itself a "one-body" problem. In this way, the EOB method provides a systematic framework for studying the dynamics of the whole binary coalescence process with the minimal usage of numerical relativity for efficiency.

Because of the nonlinearity of Einstein's gravity, the post-Newtonian (PN) Hamiltonian contains non-Coulombic higher-order interactions. Although the Newtonian two-body dynamics is integrable, the non-Coulombic potentials of the nonlinear origin naturally raise the question of the integrability of the PN inspiral dynamics. This issue may significantly challenge the matched filtering techniques [7] and has been addressed in the past decades. However, due to the complication of the PN potentials and the associated numerical calculations, the answer and the associated physical implication to gravitational wave observations are not always affirmative [8–17]. Despite that, it is known that up to 1.5PN order [i.e., up to $(v/c)^3$ terms in PN Hamiltonian], the inspiral dynamics of binary spinning black holes is integrable [4,18–21]. If the binary inspiral dynamics at higher PN orders is nonintegrable, e.g., in the presence of spin-spin interactions [22–26], then it is natural to ask how to study and characterize the chaotic behaviors arising from the

*b97202056@gmail.com
†fengli.lin@gmail.com
‡avani.physics@gmail.com

nonintegrability and how they will affect the corresponding gravitational waveforms.

The formal way of checking the integrability is to construct the commuting conserved charges in the context of symplectic dynamics [27]. If the number of such conserved charges matches the number of the dynamical degrees of freedom, then the dynamics is integrable. In practical terms, the construction is involved and may need intricate treatments, such as introducing appropriate action-angle variables, to demonstrate the (non)integrability; see for examples [19,20]. This procedure is in contrast to the construction of conserved charges of a test body moving around the background black hole metric, for which more systematic tools exist, such as the Killing-Yano tensor [28–30]. On the other hand, if the dynamics turns out to be nonintegrable, one can study the chaotic behavior by numerically evaluating the Lyapunov exponent [31], which measures the asymptotic rate of exponential separation of nearby trajectories in phase space during the time evolution. When including black hole spins, the higher number of dimensions of phase space will sometimes cause numerical ambiguity in identifying the chaotic behaviors [8,11–16]; see [32–40] for more recent discussions. This is again in contrast to the numerical characterization of chaotic behavior of a test body around a background black hole, for which the phase space is half so that the numerical evaluation takes less effort [41–47]. In fact, for the test-body case, one can reduce the phase space to a three-dimensional one[1] by adopting the energy and angular momentum conservation so that one can resort to the Birkhoff islands on Poincaré surfaces of section [48–61] to identify chaos.

By construction, the EOB dynamics is equivalent to the PN dynamics at the corresponding PN order. However, as the name of EOB suggests, it is usually assumed that the EOB dynamics is effectively a one-body one, i.e., it is a good approximation to freeze the dynamics of the background metric such as mass, spin, or position of the deformed black hole. Under such approximation, the number of degrees of freedom of the EOB dynamics is almost half of the PN ones, and the remaining degrees of freedom are just the ones of the test body. This reduction, then, will help in either formal discussion or numerical implementation of checking the integrability or characterizing the chaotic behaviors. In summary, the study of the integrability of EOB dynamics will help to reveal the approximate integrability of the corresponding PN dynamics. This approximate integrability is valid whenever the EOB dynamics with a frozen background metric is a good approximation to the original PN ones. Especially, the phase space of EOB can be reduced to three dimensional so that one can adopt the Poincaré surfaces of section and the rotation numbers to identify the chaotic behaviors. As we will demonstrate in this paper, these methods turn out to be suitable to identify chaotic behaviors of a weakly nonintegrable dynamical system, such as the dynamics of a binary system discussed throughout this paper, which can be treated as a deformed integrable system according to the Kolmogorov-Arnold-Moser (KAM) theorem [62].

This paper is outlined as follows. In Sec. II, we briefly review the EOB dynamics for spinning binaries. This section is supplemented by the Appendix, in which the EOB mapping is reviewed in more detail. In Sec. III, we show that the EOB metric does not satisfy the criterion for the existence of the Carter constant, which may imply that the geodesic dynamics of the EOB metric is nonintegrable. In Sec. IV, we identify the signatures of the chaos of the 2PN EOB dynamics by investigating the Poincaré surfaces of section and the rotation numbers of phase orbits. Possible signatures of chaos in 3PN EOB dynamics will also be discussed. We finally conclude in Sec. V.

II. A BRIEF REVIEW OF EOB DYNAMICS

The basic idea of EOB formalism is to map the two-body PN dynamics into probe dynamics moving in an "effective metric" by matching their corresponding reduced Hamilton-Jacobi functionals, which are expressed as a series of constants of motion. There are several ways to obtain the EOB dynamics; the canonical one was formulated [2] for the 2PN order of nonspinning binary black holes and later generalized to higher PN cases of spinning binaries, e.g., [5,6,63]. In particular, the EOB method adopts a particular way of relating the total energy of the two-body system $E_{\rm EOB}$ to the effective-one-body energy $E_{\rm eff}$ implied by relativistic kinematics,

$$E_{\rm eff} = \gamma\mu \quad \text{with} \quad \gamma = \frac{E_{\rm EOB}^2 - m_1^2 - m_2^2}{2m_1 m_2}, \tag{1}$$

or equivalently,

$$E_{\rm EOB} = M\sqrt{1 + \frac{2\eta}{\mu}(E_{\rm eff} - 1)}, \tag{2}$$

where $m_{1,2}$ are the masses of two black holes. The total mass, reduced mass, and the symmetric mass ratio are, respectively, given by

$$M = m_1 + m_2, \qquad \mu = \frac{m_1 m_2}{M}, \qquad \eta = \frac{\mu}{M}, \tag{3}$$

and $\gamma = 1/\sqrt{1 - \vec{v}^2}$ is the Lorentz contraction factor of the relative velocity $\vec{v}$. Note that the symmetric mass ratio η ranges from 0 to $1/4$.

[1]After imposing the conservation of energy and angular momentum, the phase space variables contain the radial variable, the polar angle, and their respective conjugate momenta. With the constraint equation from the geodesic Hamiltonian for the constant mass of the test body, the phase space is three dimensional.

Performing the EOB mapping procedure given in [4–6], one will obtain the EOB dynamics that describes a test particle moving in a deformed Kerr-like background. In the Appendix, we summarize the procedure for building the EOB mapping. In the Boyer-Lindquist coordinates $x^\mu = (t, r, y, \phi)$, the metric of the deformed Kerr-like spacetime can be formally written as

$$ds^2_{\rm eff} = g_{tt}dt^2 + g_{rr}dr^2 + g_{yy}dy^2 + g_{\phi\phi}d\phi^2 + 2g_{t\phi}dtd\phi. \tag{4}$$

For the sake of later convenience, we write down the inverse metric $g^{\mu\nu}$, whose components can be expressed as

$$g^{tt} = -\frac{g_{\phi\phi}}{g^2_{t\phi} - g_{tt}g_{\phi\phi}}, \qquad g^{t\phi} = \frac{g_{t\phi}}{g^2_{t\phi} - g_{tt}g_{\phi\phi}},$$
$$g^{\phi\phi} = -\frac{g_{tt}}{g^2_{t\phi} - g_{tt}g_{\phi\phi}}, \qquad g^{rr} = \frac{1}{g_{rr}}, \qquad g^{yy} = \frac{1}{g_{yy}}.$$

The explicit forms of these components of the inverse metric $g^{\mu\nu}$ will be given later, where they are parametrized by the total mass M, symmetric mass ratio η, and the spin parameter defined as

$$a \coloneqq \frac{|\mathbf{S}_1 + \mathbf{S}_2|}{M}, \tag{5}$$

where $\mathbf{S}_{1,2}$ are the component spins of the binary. Note that $a \leq (1-2\eta)M$, in principle, due to $|\mathbf{S}_i| \leq m_i^2$, i.e., the fulfillment of the Kerr bound for each binary component. It reduces to the extremality bound for Kerr black holes, $a \leq M$ for $\eta = 0$.

The binary dynamics is then connected to a probe dynamics of mass $\mu \coloneqq m_1 m_2/M$ moving in the above background effective metric. It can be summed up to the following effective Hamiltonian:

$$H_{\rm eff} = \beta^i p_i + \alpha\sqrt{\mu^2 + \gamma^{ij}p_i p_j + \cdots} + H^S, \tag{6}$$

where $\alpha \coloneqq 1/\sqrt{-g^{tt}}$, $\beta^i \coloneqq g^{ti}/g^{tt}$, and $\gamma^{ij} \coloneqq g^{ij} - g^{ti}g^{tj}/g^{tt}$ are, respectively, the lapse function, shift vector, and the reduced three-metric constructed from the effective metric; the $\cdots$ denotes contributions from higher than 2PN orders. We thus see that the first two terms in (6) describe a nonspinning particle of mass μ moving in the effective background with metric given by (4). The remaining H^S encodes the spin-orbital interaction and spin-spin self-interaction of the test body's spin $\mathbf{S}^*$. In [5,6] (see also the Appendix), it has been shown that $\mathbf{S}^*$ is related to the component spins of the binary $\mathbf{S}_{1,2}$ by [5,6]

$$\mathbf{S}^* \coloneqq \frac{m_2}{m_1}\mathbf{S}_1 + \frac{m_1}{m_2}\mathbf{S}_2 + \frac{1}{c^2}\mathbf{\Delta}_{\sigma^*}, \tag{7}$$

where $\mathbf{\Delta}_{\sigma^*}$ is an arbitrary vector function.[2]

The key ingredient in [2] obtaining the EOB dynamics is to further map $H_{\rm eff}$ to the so-called EOB-Hamiltonian $H_{\rm EOB}$ for the EOB dynamics. The map is inherited from (2), that is,

$$H_{\rm EOB} = M\sqrt{1 + \frac{2\eta}{\mu}(H_{\rm eff} - \mu)}. \tag{8}$$

With this identification, the resulting EOB dynamics is natural without the need to introduce additional parameters when performing the EOB mapping. For conservative dynamics without considering the radiation back reaction, we will soon see that the EOB dynamics of $H_{\rm EOB}$ is equivalent to the one of $H_{\rm eff}$.

In this paper, we would like to focus on the effect of the deformed Kerr-like background on the (non)integrability of the inspiral dynamics. Thus, we will impose the dynamical constraint $\mathbf{S}^* = 0$ by choosing an appropriate $\mathbf{\Delta}_{\sigma^*}$ so that $H^S = 0$. Note that H^S in (6) will yield the Mathisson-Papapetrou-Dixon (MPD) equation $\frac{DS^{\mu\nu}}{d\tau} = P^\mu u^\nu - P^\mu u^\nu$ with the linear momentum $P^\mu = \mu u^\mu + \mathcal{O}((\mathbf{S}^*)^2)$ with u^μ the four-velocity of the probe particle. After imposing supplementary spin conditions (e.g., see [64] for interesting discussions), the MPD equation can be reduced to $\frac{D\mathbf{S}^*}{d\tau} = \mathcal{O}((\mathbf{S}^*)^2)$ [65]. Therefore, if we choose $\mathbf{S}^* = 0$ right from the beginning by properly tuning (7), we can consistently turn off the probe's spin. For simplicity, in this paper, we will consider only the case with $\mathbf{S}^* = 0$ up to 2PN order. That is, we will consider the following effective Hamiltonian:

$$H_{\rm eff} = \beta^i p_i + \alpha\sqrt{\mu^2 + \gamma^{ij}p_i p_j}. \tag{9}$$

This effective Hamiltonian describes the geodesic motion of a nonspinning probe of mass μ moving in the deformed Kerr background metric (4).

We will show that the EOB dynamics based on the above effective Hamiltonian will yield resonant islands/Birkhoff islands on the Poincaré surfaces of section even for the probe without spin. The resonant islands/Birkhoff islands we will obtain are due to the deformation from the exact Kerr metric contributed by the nonzero symmetric mass ratio η. This is in contrast to the chaotic orbits of a spinning probe moving around a Kerr black hole [44,46].

[2]The EOB mapping between $\mathbf{S}^*$ and a (background spin parameter) and component spins $\mathbf{S}_{1,2}$ is not unique. Different mappings are related by canonical transformations and redefinitions of the Hamilton-Jacobi function [5,6]. However, in either EOB frame, we can have $\mathbf{S}^* \coloneqq \frac{m_2}{m_1}\mathbf{S}_1 + \frac{m_1}{m_2}\mathbf{S}_2$ by setting the arbitrary function $\mathbf{\Delta}_{\sigma^*}$ to some appropriate specific form.

The investigation of inspiraling dynamics similar to that of Eq. (9) has also been performed [66,67], in which the authors considered extreme mass-ratio limit, i.e., $\eta \ll 1$, and focused on equatorial-eccentric orbits and generic orbits, respectively. In Refs. [66,67], the probe spin effects are omitted because of the extreme mass-ratio limit. In addition, in the same limit, one can define an approximated Carter constant, and the system becomes approximately integrable. This is not the case in the scenarios that we will consider here. We will go beyond the extreme mass-ratio limit and investigate how an arbitrary η generates chaotic behaviors in the EOB framework.

The effective metric (4) is stationary and axisymmetric, so that $H_{\rm EOB}$ and p_ϕ are constants of motion, which we will denote as E_T and L_z, respectively. In the EOB framework, the reduced mass μ and the symmetric mass ratio η are also dynamically constant. Equation (8) thus implies that $H_{\rm eff}$ is also a constant of motion, which we denote as E. Thus, E_T and E are related by

$$E_T = M\sqrt{1+\frac{2\eta}{\mu}(E-\mu)}. \tag{10}$$

The Hamilton equations of $H_{\rm EOB}$ are then given by

$$\frac{dq^i}{dt_{\rm EOB}} = \frac{\partial H_{\rm EOB}}{\partial p_i} = \frac{M}{E_T}\frac{\partial H_{\rm eff}}{\partial p_i} = \frac{M}{E_T}\frac{dq^i}{dt}, \tag{11}$$

$$\frac{dp_i}{dt_{\rm EOB}} = -\frac{\partial H_{\rm EOB}}{\partial q^i} = -\frac{M}{E_T}\frac{\partial H_{\rm eff}}{\partial q^i} = -\frac{M}{E_T}\frac{dp_i}{dt}, \tag{12}$$

where we have used (8) and the constraint

$$H_{\rm EOB} = E_T \tag{13}$$

to arrive at the second equalities. From the above, i.e., the second equalities in (11) and (12), it is clear that we can map the Hamiltonian dynamics of $H_{\rm EOB}$ into the one of $H_{\rm eff}$ by simply rescaling the time coordinate with a factor E_T/M and at the same time replacing the constraint (13) by

$$H_{\rm eff} = E, \tag{14}$$

with E relating to E_T by (10).

Since the EOB dynamics and effective dynamics are equivalent for finite fixed energy by a simple rescaling of the time coordinate, in the following we will analyze the phase space for the effective dynamics or its associated geodesic dynamics, and the result should also hold for the EOB dynamics.

III. (NON)INTEGRABILITY OF EOB DYNAMICS

Before solving the aforementioned nonspinning EOB dynamics for the binary Kerr black holes or the equivalent geodesic dynamics in the spacetime described by the effective metric (4), we would like to examine whether the corresponding system is integrable or not. The fact that EOB dynamics can be described as the geodesic motion of a test particle around an effective metric allows us to check the integrability of the system by examining the (non) existence of the Carter constant of the effective metric. We follow the criterion given in [29,68], which is applied to a metric with two commuting Killing vectors. If a metric satisfies the criterion, the geodesic equations can be separated, and the corresponding dynamics is integrable. The criterion [29] essentially states that the existence of the Carter constant requires the (inverse) metric to take the following Papadopoulos-Kokkotas (PK) form in the Boyer-Lindquist coordinates:

$$\begin{aligned} g^{tt} &= \frac{\mathcal{A}_5(r)+\mathcal{B}_5(y)}{\mathcal{A}_1(r)+\mathcal{B}_1(y)}, & g^{t\phi} &= \frac{\mathcal{A}_4(r)+\mathcal{B}_4(y)}{\mathcal{A}_1(r)+\mathcal{B}_1(y)}, \\ g^{rr} &= \frac{\mathcal{A}_2(r)}{\mathcal{A}_1(r)+\mathcal{B}_1(y)}, & g^{yy} &= \frac{\mathcal{B}_2(y)}{\mathcal{A}_1(r)+\mathcal{B}_1(y)}, \\ g^{\phi\phi} &= \frac{\mathcal{A}_3(r)+\mathcal{B}_3(y)}{\mathcal{A}_1(r)+\mathcal{B}_1(y)}, \end{aligned} \tag{15}$$

where $\mathcal{A}_i(r)$ and $\mathcal{B}_i(y)$ are arbitrary functions of r and y.

The explicit form of the inverse metric associated with (4) for the 2PN-order EOB dynamics can be found in [5,69], and we just write down here

$$\begin{aligned} g^{tt} &= -\frac{\Lambda_t}{\Delta_t\Sigma}, & g^{t\phi} &= -\frac{\tilde{\omega}_{fd}}{\Delta_t\Sigma}, & g^{rr} &= \frac{\Delta_r}{\Sigma}, \\ g^{yy} &= \frac{1-y^2}{\Sigma}, & g^{\phi\phi} &= \frac{1}{\Lambda_t}\left(-\frac{\tilde{\omega}_{fd}^2}{\Delta_t\Sigma}+\frac{\Sigma}{1-y^2}\right), \end{aligned} \tag{16}$$

where

$$\begin{aligned} &\Delta_t = \Delta + \eta F(r), \qquad \Delta_r = \Delta_t[1+\eta G(r)], \\ &\tilde{\omega}_{fd} = a(X-\Delta)[1+\eta H(r)], \\ &\Lambda_t = X^2 - a^2\Delta_t(1-y^2), \end{aligned} \tag{17}$$

with

$$\Sigma = r^2 + a^2y^2, \qquad \Delta = r^2 - 2Mr + a^2, \qquad X = r^2 + a^2, \tag{18}$$

and

$$\begin{aligned} F(r) &= \frac{2M^3}{r}, \\ G(r) &= \frac{1}{\eta}\ln\left[1+6\eta\frac{M^2}{r^2}\right], \\ H(r) &= \frac{1}{2r^2}(\omega_1^{fd}M^2 + \omega_2^{fd}a^2). \end{aligned} \tag{19}$$

The parameters $\omega_{1,2}^{fd}$ in the last line of (19) are adjustable to regulate the strength of frame dragging. Note that, at 1PN

order, the EOB metric (16)–(19) will simply reduce to the one of the Schwarzschild black hole [4]. Moreover, one can determine the extremality bound $a_{\rm ext}(\eta)$ by requiring $r\Delta_t(r) = (r-r_1)^2(r-r_2)$ for $r_1 > 0$ when $\eta \in [0, 1/4]$, so that $a_{\rm ext}(\eta) = \sqrt{r_1^2 - 2r_1 r_2}$. Then, it is straightforward to see that $a_{\rm ext}(\eta) \geq (1-2\eta)M$. Thus, the metric (19) always admits an event horizon whenever the Kerr bound holds for both binary components.

Given the above effective metric of EOB dynamics, we can check if it can be recast into the PK form. We immediately can identify

$$\begin{aligned}
&\mathcal{A}_1(r) = r^2, \qquad \mathcal{B}_1(y) = a^2y^2,\\
&\mathcal{A}_2(r) = \Delta_r, \qquad \mathcal{B}_2(y) = 1-y^2,\\
&\mathcal{A}_5(r) = -\frac{X^2}{\Delta_t}, \qquad \mathcal{B}_5(y) = a^2(1-y^2),\\
&\mathcal{A}_4(r) = -\frac{a(X-\Delta)[1+\eta H(r)]+\Delta_t}{\Delta_t}, \qquad \mathcal{B}_4(y) = 1.
\end{aligned} \tag{20}$$

This then gives the constraint

$$\mathcal{A}_3(r) + \mathcal{B}_3(y) = \frac{1}{1-y^2} - \frac{a^2}{\Delta_t} - \frac{\eta a^2(X-\Delta_t+(X-\Delta)[1+\eta H(r)])((X-\Delta)H(r)+F(r))}{\Delta_t[X^2 - a^2\Delta_t(1-y^2)]}. \tag{21}$$

The third term involves nonseparable r, y dependence so that it is not possible to find appropriate $\mathcal{A}_3(r)$ and $\mathcal{B}_3(y)$ to satisfy the above constraint. However, this term vanishes for either $a = 0$ or $\eta = 0$. The $\eta = 0$ is the probe limit that can be treated as a probe moving around the Kerr black hole whose geodesics are integrable. On the other hand, $a = 0$ holds only for the nonspinning binary black holes. The EOB metric becomes a deformed Schwarzschild metric with modified harmonic function but remains spherically symmetric so that the geodesic dynamics is integrable by having an additional Carter constant. Therefore, the generic 2PN EOB dynamics does not contain a second-order Killing tensor according to the PK criterion. This is consistent with the results of Ref. [67]. It should be emphasized that, although a second-order Killing tensor does not exist, it does not exclude the possibility of the existence of higher-order Killing tensors that make the dynamics integrable. Therefore, in order to check nonintegrability of the dynamics, we need to resort to numerical integrations of geodesic equations and find chaotic signatures. This is what we will carry out in the next section.

There are general discussions on the integrability of PN inspiral dynamics [8–11,14,16,17,19,20], and it is known that inspiral dynamics up to 1.5PN is integrable. This is consistent with the PK criterion for the EOB dynamics at 1PN, for which the EOB metric is a pure Schwarzschild one, i.e., $a = \eta = 0$, and at 1.5PN with vanishing test particle spin, for which $a \neq 0$ but $\eta = 0$. This suggests that one can deal with the integrability issue of PN inspiral dynamics in the equivalent EOB formalism with the advantage of reducing the two-body phase space to the one-body one.

IV. CHAOTIC SIGNATURES OF THE EOB DYNAMICS

As discussed in Sec. II, the EOB dynamics based on $H_{\rm EOB}$ of (8) (up to 2PN order with zero probe spin $\mathbf{S}^*$) is equivalent to the dynamics based on $H_{\rm eff}$ of (9). The latter is nothing but the Hamiltonian formulation of a test particle of mass μ moving in the background geometry described by the metric (16). Therefore, in this section, we will focus on the geodesic dynamics of a test particle moving in the effective metric (16). Then, we will exhibit the signatures of chaos in the system using the Poincaré surfaces of section and the concepts of rotation curves.

A. Theoretical setup: Poincaré surface of section and Birkhoff islands

The dynamics of a massive test particle moving in the effective metric (16) can be obtained by solving the geodesic equations of this metric. Because the effective metric is stationary and axisymmetric, namely, the metric functions do not depend explicitly on t and ϕ, one can define two corresponding constants of motion E and L_z. These two constants of motion represent the energy and the azimuthal angular momentum, respectively, and one can use them to obtain the following two equations of motion:

$$\dot{t} = -g^{tt}E + g^{t\phi}L_z, \tag{22}$$

$$\dot{\phi} = -g^{t\phi}E + g^{\phi\phi}L_z, \tag{23}$$

where the dot denotes the derivative with respect to the proper time τ. The evolution of r and y sectors is governed by two coupled second-order differential equations, subject to a Hamiltonian constraint, which is associated with the conservation of the rest mass of the test particle. This constraint can be written as

$$\dot{r}^2 + \frac{g^{rr}}{g^{yy}}\dot{y}^2 + V_{\rm eff} = 0, \tag{24}$$

where the effective potential reads

$$V_{\rm eff} = g^{rr}(1 + g^{tt}E^2 + g^{\phi\phi}L_z^2 - 2g^{t\phi}EL_z). \tag{25}$$

The values of energy E and azimuthal angular momentum L_z will be normalized with the reduced mass μ throughout this paper.

Using the constraint equation (24), one can define the so-called the curve of zero velocity (CZV) as

$$V_{\rm eff} = 0, \tag{26}$$

on which both the radial and angular velocities are zero. CZV determines the boundary of a set of allowed orbits in spacetime. In Fig. 1, we show some typical CZVs in the (r, y) plane for $\eta = 0.15$ and different values of spin parameter a, E, and L_z. For simplicity, we also set $\omega^{fd}_{1,2}$ of (19) to zero in this paper. For this chosen η, the extremality bound for the metric (19) is $a \leq a_{\rm ext}(\eta = 0.15) = 0.847\ M$, and the requirement from the component Kerr bound gives $a \leq (1 - 2\eta)M = 0.7\ M$. Figure 1(a) shows the CZV with $E = 0.942$ and $L_z = 2.76\ M$ in the effective metric with $a = 0.67\ M < 0.7\ M$, which admits an event horizon at $r = 1.60\ M$. We see that, in this case, the CZV forms a closed region in which the bound orbits reside. Near the event horizon (red dashed line), a second branch of CZV encloses a small region of plunging orbits. Figure 1(b) shows the CZVs with $E = 0.93671$ and $L_z = 1.7542M$ around two corresponding effective metrics that differ only by the spin a, i.e., $a = 0.69\ M$ and $a = 0.86\ M$. The metric for $a = 0.69\ M$ admits an event horizon, but not for $a = 0.86\ M$; i.e., it corresponds to a naked singularity. We see that the CZV around the effective metric with $a = 0.86\ M$ forms a closed curve representing the boundary of a set of bound orbits. On the other hand, the CZV around the effective metric with $a = 0.69\ M$ does not form a closed curve but ends on the horizon. This throatlike CZV connects the region of bound orbits to the plunging region.

The geodesic equations of test particles moving around a Kerr spacetime are integrable. The integrability of this system results from the existence of a hidden symmetry of the spacetime that allows one to define a Carter constant $\mathcal{K}$. Technically, this constant can be identified as a decoupling constant when separating the radial sector of the geodesic equations from the sector of polar angle. As an integrable system, the phase orbits of particles moving around the Kerr spacetime lie on two-dimensional tori in phase space. Each torus is characterized by specific values of constants of motion (E, L_z, $\mathcal{K}$, and the mass of the test particle) and, consequently, by orbital frequencies and their ratio. In particular, the orbits, in this case, oscillate in both the radial and latitudinal directions, with characteristic frequencies given by ω_r and ω_θ, respectively. The ratio of these frequencies is called the rotation number $\nu_\theta \equiv \omega_r/\omega_\theta$. If the rotation number of an orbit is rational, the orbit is periodic, forming closed curves on the torus. Orbits of this type are called resonant orbits. On the other hand, if ν_θ is irrational, the orbits can cover the torus densely and are called quasiperiodic. It turns out that the rotation number can be used to classify orbits. Most importantly, it can also identify the signatures of chaos, even if the chaotic behaviors are very weak.

The integrable geodesic motion bears geometric features in the reduced phase space by constructing the Poincaré map, see, e.g., [31]. To proceed, one cuts a surface through

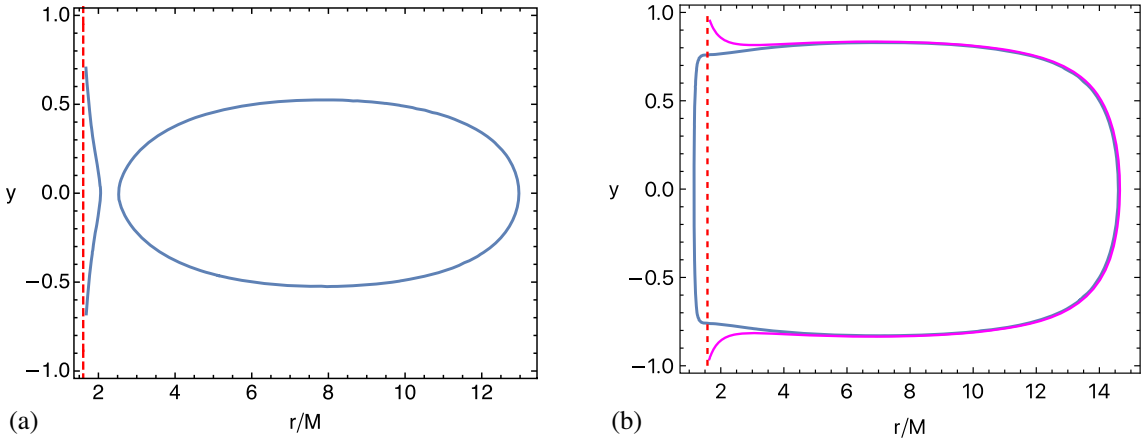

FIG. 1. The typical CZVs of the 2PN EOB metrics with $\eta = 0.15$ and $\omega^{fd}_1 = \omega^{fd}_2 = 0$ for different values of spin parameter a, test particle's energy E, and azimuthal angular momentum L_z measured in the unit of reduced mass μ. The event horizon, if it exists, is indicated by the red dashed line. (a) The CZV with $E = 0.942$, $L_z = 2.76\ M$ around the effective metric with $a = 0.67\ M$ forms a closed region, but there appears a second nonclosed branch near the horizon. (b) Two CZVs with $E = 0.93671$ and $L_z = 1.7542\ M$ around the effective metric spin $a = 0.86\ M$ (blue) and $a = 0.69\ M$ (magenta). Note that the two CZVs here overlap each other for larger r but differ significantly at small r. Because of the 2PN correction, the extremality bound for the absence of naked singularity for the EOB metric is no longer $a \leq M$ but $a \leq a_{\rm ext}(\eta) < M$. For $\eta = 0.15$, $a_{\rm ext} = 0.847\ M$. Thus, the metric with $a = 0.86\ M$ does not admit an event horizon, such that the naked singularity appears, but the CZV is closed in this case. The CZV with $a = 0.69\ M$ in (b) has a throatlike shape and connects to the horizon.

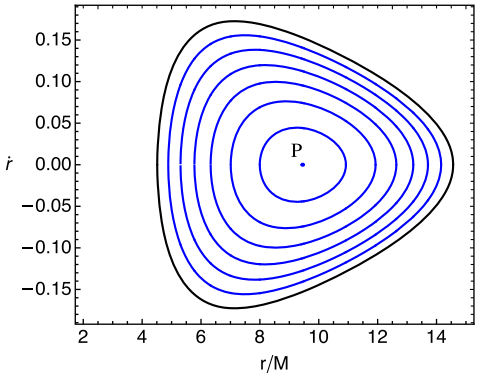

FIG. 2. Poincaré surface of section of the integrable geodesic motion in the Kerr spacetime. Each invariant curve (blue) corresponds to a specific value of the Carter constant. Here, we choose $E = 0.95$, $L_z = 3\ M$, and $a = 0.9\ M$.

the foliage of the tori on which the corresponding quasiperiodic orbits densely cover as time goes on, and then each of such tori makes a closed curve on the surface. This surface and the closed curves constructed above are called Poincaré surfaces of section and invariant curves, respectively. Typical invariant curves for Kerr geodesics of different values of $\mathcal{K}$ but fixed E, L_z, and a are shown in Fig. 2. The Poincaré surface of section shown here is chosen to be the equatorial plane, i.e., $y = 0$. We plot the intersections of orbits when they pierce through the equatorial plane with a positive y direction. The black contour is defined by $\dot{y} = 0$ and shows the boundary of bound orbits. As shown, the invariant curves are continuous and different curves corresponding to different values of $\mathcal{K}$ are nested within each other [70].

If the integrable system is perturbed by nonintegrable deformations, as in the case of EOB dynamics that can be treated as geodesic dynamics in a deformed Kerr metric, the system becomes chaotic. Essentially, the behavior of orbits in the phase space depends on whether the deformations are large or not. If the deformations are large, strong chaos may appear, and the whole phase space portrait could be significantly destroyed. However, if the deformations are small, according to the KAM theorem [31,62], most of the tori remain undestroyed except for those corresponding to the resonant orbits. Correspondingly, the original invariant curves on the Poincaré surfaces of section become slightly deformed but remain continuous. They are called KAM curves.

For resonant orbits, the situations become more complicated. According to the Poincaré-Birkhoff theorem [31,71], the tori on which resonant orbits are located may dissolve after nonintegrable deformations enter. Correspondingly, the resonant points on the Poincaré surfaces of section would be split into a number of periodic points, with half of them stable and the other half unstable. Around the stable periodic points, small islands of nested KAM curves appear, which are called Birkhoff chains of islands. For the orbits within the islands, the rotation numbers should be equal to those of the resonant orbits in the original integrable system. The rotation number of an orbit starting with a given initial condition can be operationally obtained by the limiting formula [31,72]

$$\nu_\theta = \lim_{N\to\infty} \frac{1}{2\pi N} \sum_{i=1}^{N} \vartheta_i, \tag{27}$$

where ϑ_i is the angle between the position vectors of two successive piercings of the given orbit on the Poincaré surface of section. The position vectors are defined with respect to the central fixed point P, which is defined by the unique piercing of the orbit that only crosses through the surface once (we show a central point P in Fig. 2). In practice, we can obtain a well-approximated value of ν_θ for large enough N. The appearance of Birkhoff islands in Poincaré surfaces of section is a clear signature of chaos in the system, and it will result in rational plateaus in the rotation curve. That is, ν_θ will show plateaus at rational values such as $1/2$, $2/3$, etc., when varying the initial conditions.

B. Birkhoff islands of EOB orbits

In this section, we investigate the breaking up of tori in a Poincaré section of the phase space, treating the geodesic motion in the effective metric of (16) as a perturbation to the integrable Kerr system. As mentioned in Sec. II, the effective metric (16) is parametrized by mass M, spin parameter a, and symmetric mass ratio η. Therefore, different values of these parameters along with the choice for energy E and angular momentum L_z of the test particle may affect the degree of chaos exhibited by trajectories of phase orbits on Poincaré surfaces of section. To identify chaotic features using this approach, we numerically integrate the Hamilton equations given by the geodesic dynamics of the effective metric (16). While solving the equations, we keep the constraint equation (24) being satisfied down to 10^{-8} during the whole integration using the standard Runge-Kutta eighth-order method. Each trajectory is integrated until its characteristic patterns on the Poincaré surface of section robustly appear, e.g., continuous KAM curves, clear Birkhoff chains of islands, etc. The integration time varies among different trajectories. Normally, the integration lasts for up to $10^3 \sim 10^4$ periods for each trajectory.

We first consider the case where $a < (1 - 2\eta)M$ such that each of the two binaries satisfies the Kerr bound. More explicitly, we consider the 2PN EOB metric with $a = 0.67\ M$ and $\eta = 0.15$, then we set $E = 0.942$ and $L_z = 2.76\ M$. A slight change of E and L_z will not affect the qualitative behaviors of our results. The results are shown in Fig. 3. In Fig. 3(a), one sees a closed KAM curve (green), which is associated with an irrational-ν_θ quasiperiodic orbit.

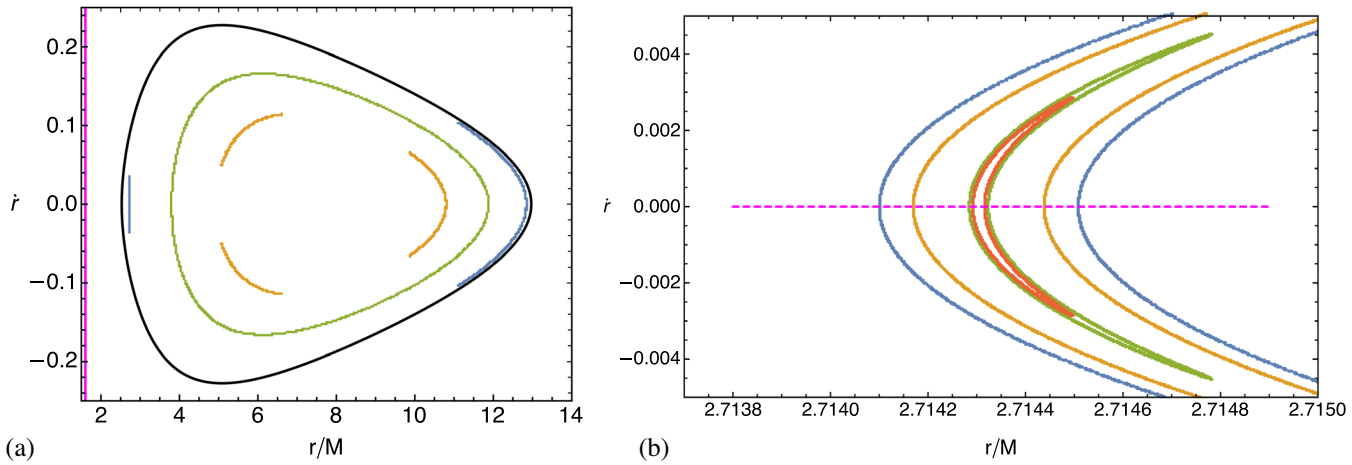

FIG. 3. Poincaré surface of section for geodesic motions in the EOB metric (16) for the spin parameter $a = 0.67\ M$, symmetric mass ratio $\eta = 0.15$, energy $E = 0.942$, and azimuthal angular momentum $L_z = 2.76\ M$. (a) Birkhoff islands (blue, $1/2$ resonance; orange, $2/3$ resonance) and one KAM curve (green). The vertical magenta line indicates the event horizon. (b) Enlargement of the left branch of the $1/2$-resonant islands.

In addition, two sets of chains of Birkhoff islands can be clearly identified. They correspond to rational-ν_θ resonant orbits. In Fig. 3(a), we show the islands that correspond to $1/2$- (blue) and $2/3$-resonant orbits (orange). The detailed structure of the left branch of the $1/2$-resonant islands is exhibited in the enlargement, Fig. 3(b). The Birkhoff islands come from the splitting resonant points with rational ν_θ, and chaotic behaviors should be characterized by the discontinuity of ν_θ when varying the initial conditions, as suggested by the KAM theorem and Poincaré-Birkhoff theorem.

Using the operational method of (27), we can specifically consider a collection of orbits whose initial conditions are parametrized by $(r_0, y_0, \dot{r}_0) = (r, 0, 0)$. The initial points of these orbits correspond to a set of piercings of the orbits through the equatorial plane with zero radial velocities. This set of piercings appears as a horizontal line on the Poincaré surface of section. We can then draw the so-called rotation curve, which is defined by the rotation numbers as a function along with this set of initial conditions, that is, as a function of r. In Fig. 4(a), we choose a set of orbits whose initial points correspond to the magenta dashed line in Fig. 3(b) and calculate their rotation numbers. As one can see from this figure, when the orbits are inside the island, their rotation numbers are nearly a constant, forming a plateau in the rotation curve. More explicitly, we see that the rotation number monotonically

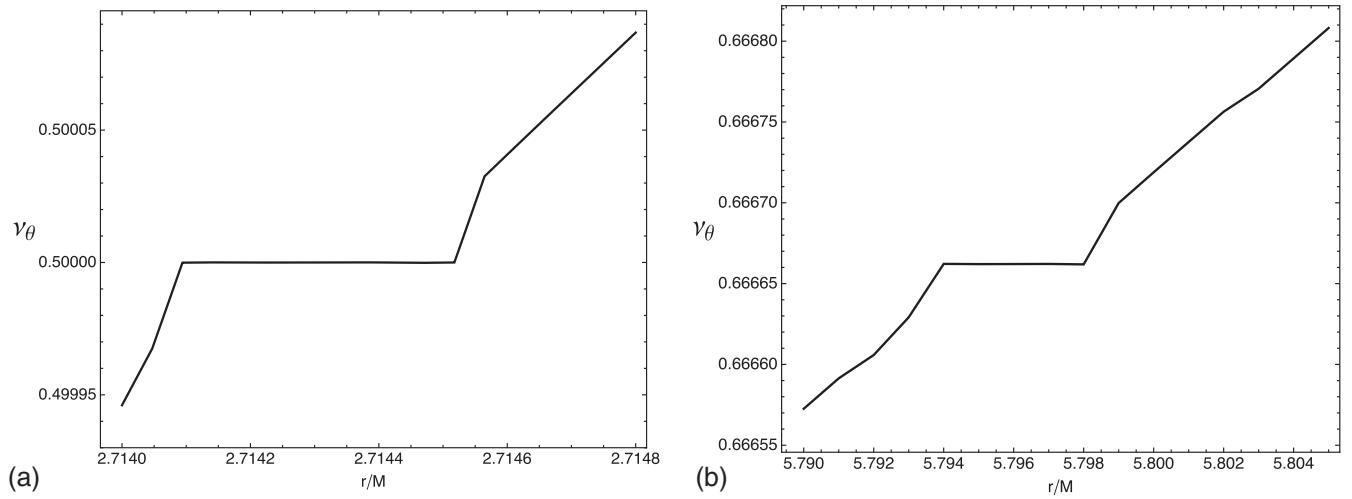

FIG. 4. (a) The rotation curve drawn along the magenta dashed line in Fig. 3(b). The plateau has a constant rotation number $\nu_\theta = 1/2$ and corresponds to the $1/2$-resonant Birkhoff islands shown in Fig. 3. (b) The rotation curve drawn along a horizontal line in Fig. 3(a) that crosses the upper-left branch of the $2/3$-resonant islands. The plateau appears as shown in both cases because the rotation number remains a constant when crossing an island.

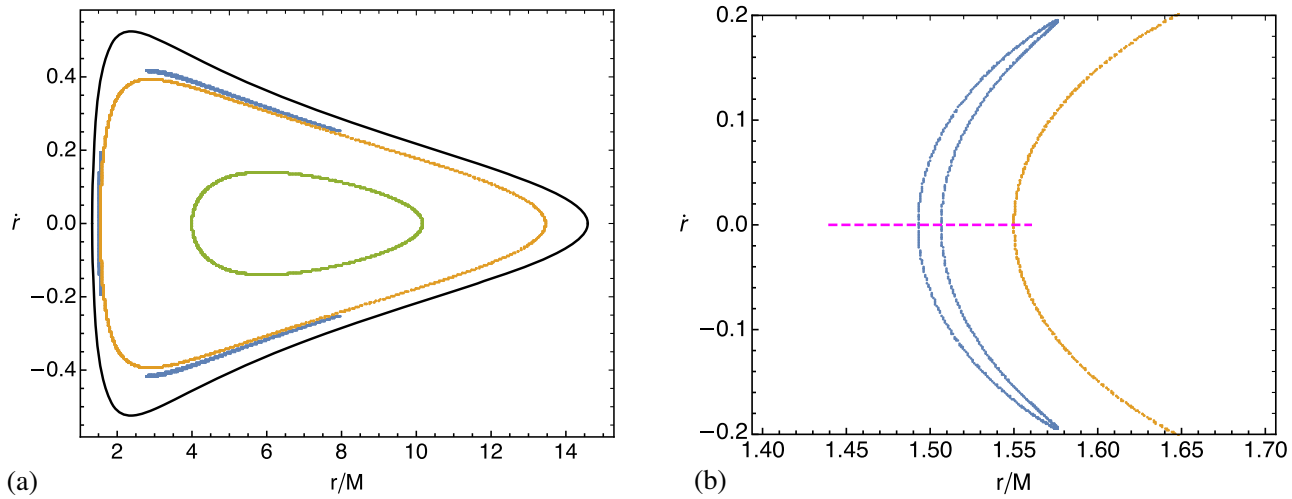

FIG. 5. Poincaré surface of section for geodesic motions in the EOB metric (16) for the spin parameter $a = 0.92\ M$, symmetric mass ratio $\eta = 0.15$, energy $E = 0.9367$, and azimuthal angular momentum $L_z = 1.7542\ M$. (a) KAM curves and Birkhoff islands (2/3 resonance) for initial conditions $(r_0, y_0, \dot{r}_0) = (1.493\ M, 0.1, 0)$ (blue), $(1.55\ M, 0, 0)$ (orange), and $(4\ M, 0, 0)$ (green). (b) Enlargement of the 2/3-resonant Birkhoff island (blue) with initial condition $(r_0, y_0, \dot{r}_0) = (1.493\ M, 0.1, 0)$. A nearby KAM curve is also shown (orange).

increases with r except for a finite range of radii in which ν_θ remains unchanged. The constant value of rotation number, i.e., $\nu_\theta = 1/2$ at the plateau, indicates that the islands in blue in Fig. 3(a) correspond to the "1/2" resonance of phase orbits. On the other hand, in Fig. 4(b), we consider a set of orbits whose initial points form a horizontal line on Fig. 3(a) that crosses the upper-left branch of the 2/3-resonant islands. The rotation curve has a clear plateau on which the rotation number remains at $\nu_\theta = 2/3$. The existence of Birkhoff islands and plateaus in the rotation curve are clear signatures of chaos.

While scanning the parameter space, we find that with higher values of spin parameter a and symmetric mass ratio η, the chaotic tendency of phase orbits becomes stronger. The effects would be even more profound when the extremality bound is violated, i.e., $a > a_{\rm ext}(\eta)$. This motivates us to investigate in more details the phase orbits in these configurations. Although these configurations may not be strictly physical due to the existence of naked singularities, they can provide us with some insights about how the extremely rapid spins could enhance the chaotic nature of the system. Therefore, we now consider the 2PN EOB metric with $a = 0.92\ M$ and $\eta = 0.15$. We hereafter will set the fixed values for $E = 0.9367$ and $L_z = 1.7542\ M$ for the 2PN cases. Again, a slight change of these constants of motion does not affect the qualitative results discussed below. The results are shown in Fig. 5.

In Fig. 5, we can see the features of KAM curves associated with the irrational-ν_θ quasiperiodic orbits and obtained by different initial conditions, i.e., the closed curves with different colors (orange/green). In addition, in the enlargement, Fig. 5(b), we can again clearly see the features of Birkhoff islands associated with rational-ν_θ resonant orbits. As the strength of the nonintegrability is characterized by the combined effect of a and η, we later will see that, with fixed E and L_z, the strength of chaotic behaviors of the system would be enhanced when a and η increase.

In Fig. 6, we choose a set of orbits whose initial conditions correspond to the magenta dashed line in Fig. 5(b) and calculate their rotation numbers. As one can see from this figure, when the orbits are inside the island, i.e., the region enclosed by the blue curve in Fig. 5(b), the rotation curve has a plateau. Indeed, the rotation number monotonically decreases with r except for a finite range of radius around $r = 1.5\ M$ in which ν_θ remains unchanged. The constant value of rotation number, i.e., $\nu_\theta = 2/3$, at the plateau

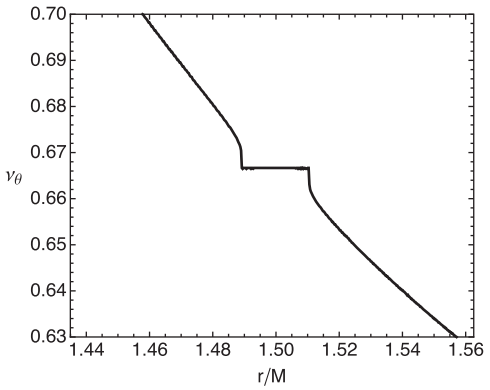

FIG. 6. The rotation curve drawn along the magenta dashed line in Fig. 5(b), in which $\eta = 0.15$ and $a = 0.92\ M$. The plateau around $r = 1.50\ M$ corresponds to the 2/3-resonant Birkhoff island shown in Fig. 5(b).

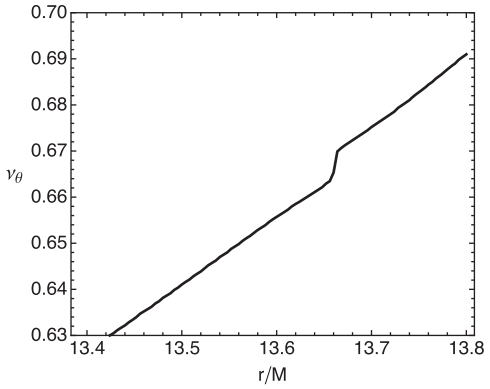

FIG. 7. The abrupt change in the rotation curve at $\nu_\theta = 2/3$ corresponds to the region near an unstable periodic orbit.

indicates that the three branches of islands (shown in blue) in Fig. 5 correspond to the "2/3" resonance of phase orbits.

In addition to plateaus that indicate the existence of Birkhoff islands, there is another feature in rotation curves that also indicates chaos in a dynamical system. In Fig. 7, we consider the same EOB metric and constants of motion E and L_z as those in Fig. 6, but draw the rotation curve in a different range of r. As one can see in this figure, instead of a plateau, the rotation curve could be featured by an abrupt change. In this case, the abrupt change at $\nu_\theta = 2/3$ corresponds to the region near an unstable point. Near this region, the tori structure is only deformed, compared with the original invariant curves, but not yet destroyed.

In fact, rotation curves can be used not only as a tool to search for chaos in the dynamical system, but also to locate the Birkhoff islands in the Poincaré surfaces of section. In particular, the islands that correspond to higher-order resonances are typically very thin and are difficult to identify. For example, one can first calculate the rotation curve along the whole horizontal axis ($\dot{r} = 0$) within CZV and find the short range of radius r that is associated with a rational ν_θ. These radii should correspond to the initial conditions r_0 of the orbits that cross the islands, if islands exist. This method can substantially assist in finding islands of high resonances. In Fig. 8 we consider $a = 0.86\ M$ and $\eta = 0.15$, then exhibit the Birkhoff islands of $2/3$ (blue), $1/2$ (orange), $2/5$ (red), and $1/3$ resonances (green). The inset shows the enlargement of these islands near the left edge of the Poincaré surface of section. The rotation curve along the horizontal magenta line is shown in Fig. 9. The plateaus appear when the orbits cross the islands, with the

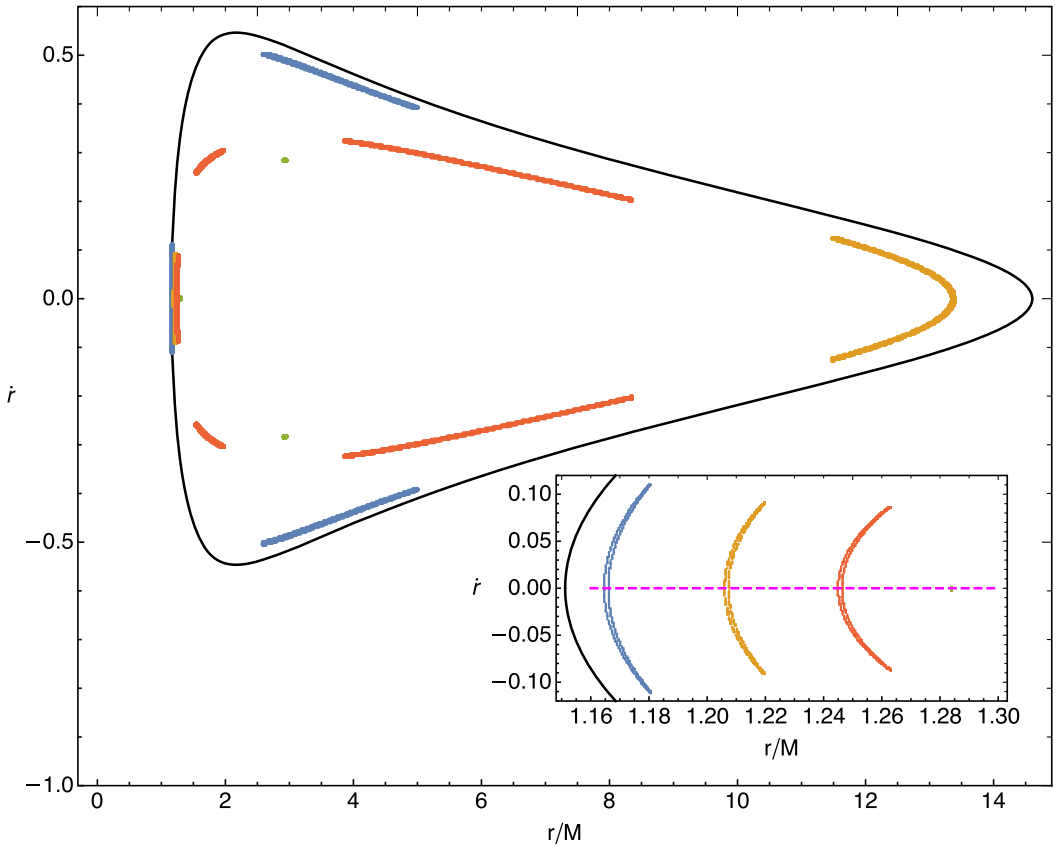

FIG. 8. Birkhoff chains of islands for 2PN Hamiltonian for $\eta = 0.15$ and $a = 0.86\ M$. Inset: Enlargement of the islands on the left edge of the Poincaré surface of section, which consists of $2/3$ (blue), $1/2$ (orange), $2/5$ (red), and $1/3$ resonances (green).

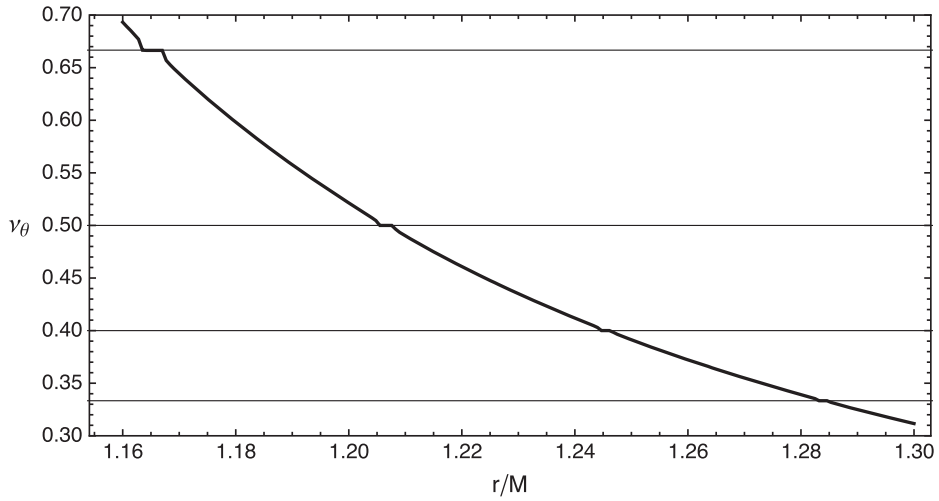

FIG. 9. The rotation curve drawn along the horizontal magenta line in the inset of Fig. 8. Plateaus that correspond to different orders of resonances are clearly visible.

rotation numbers being $2/3$, $1/2$, $2/5$, and $1/3$, from left to right, respectively.

Before closing this subsection, we would like to investigate how the strength of chaos is affected by the interplay of the metric parameters a and η when fixing E and L_z. This can be done using the Poincaré surface of section. First, we fix $E = 0.9367$ and $L_z = 1.7542\ M$, then we consider the $\{a, \eta\}$ configuration where the extremality bound is violated. We choose this configuration because its island structures are more apparent and easier to identify. We focus on the leftmost branch of the $2/3$-resonant islands, e.g., the blue islands in Fig. 5. This branch of islands is always vertically symmetric with respect to the $\dot{r} = 0$ axis. Therefore, it is convenient to use the width on the $\dot{r} = 0$ axis of this branch of islands as a measure of the strength of chaos in the system. For a given value of the symmetric mass ratio η, we define the critical value of spin parameter $a_{\rm cri}$ below which the width δr of the leftmost $2/3$-resonant island is smaller than $0.001M$. For fixed values of E and L_z, the value of $a_{\rm cri}$ varies with η, and the results of fixing $E = 0.9367$ and $L_z = 1.7542\ M$ are shown by the black points for some chosen η in Fig. 10, which fit very well with a linear function (blue dashed line). From this figure, we find that $a_{\rm cri}$ decreases with increasing symmetric mass

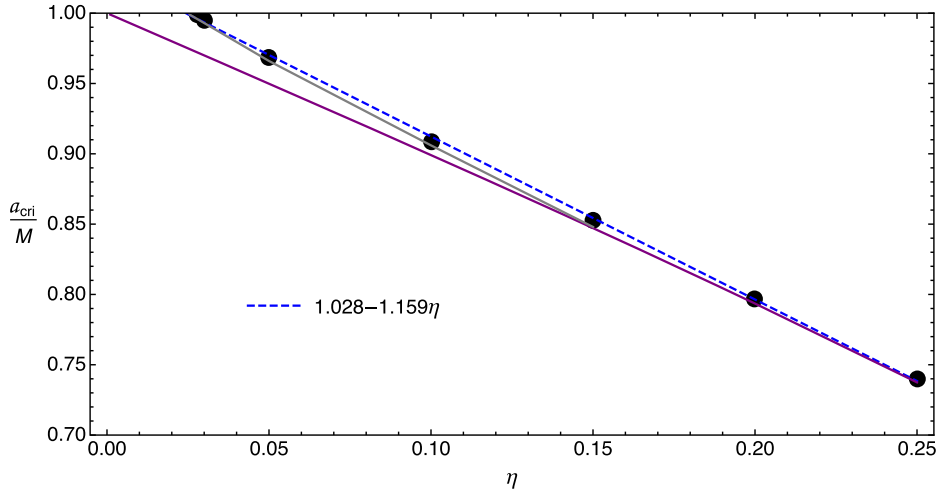

FIG. 10. The critical spin $a_{\rm cri}$ for some values of the symmetric mass ratio η (black points) upon fixing $E = 0.9367$ and $L_z = 1.7542\ M$. The points fit very well with a linear function (blue dashed line). Below the blue dashed line or the gray curve, the leftmost $2/3$-resonant island either disappears or becomes too small to measure. Also, the extremality bound $a_{\rm ext}(\eta)$ is shown by the purple curve. Note that $a_{\rm cri}$ as a function of η depends also on the choice of E and L_z. We can also observe that the case with closed CZV in Fig. 1(b) lies above the blue dashed line and one with open CZV resides below it. For this particular choice of E and L_z, the above three curves are near to each other, which makes it interesting to explore the role played by the event horizon in formation or destruction of islands.

ratio η, meaning that the strength of chaos increases when the values of a and η increase. In this figure, we also show a gray curve on which the rotation numbers on the left edge of CZV are $2/3$. Therefore, below the gray curve, the $2/3$-resonant islands do not appear within CZV. In addition, we show the extremality bound $a_{\rm ext}(\eta)$ using the purple curve. Although in Fig. 10 we only focus on the parameter space in which the extremality bound is violated, we should emphasize that the chaotic signatures such as Birkhoff islands and plateaus in rotation curves also appear when the extremality bound is satisfied. As we have shown in Figs. 3 and 4, upon another choice of E and L_z, chaotic signatures also appear when each binary is below the Kerr bound, i.e., $a < (1-2\eta)M$. The islands found there may just be too thin to be detectable in the real gravitational wave events. We consider the configuration that violates the extremality bound in Fig. 10 mainly because the island structures are easier to identify in this configuration. Furthermore, the critical spin $a_{\rm cri}$ for a given η depends on the values of E and L_z as well. How $a_{\rm cri}$ would be altered when the parameters η, E, and L_z are all allowed to change is not a trivial question. The main conclusion we would like to draw from Fig. 10 is that the chaotic behaviors of the system, when fixing E and L_z, are enhanced with a and η. This conclusion is expected to hold also for the configuration where $a < (1-2\eta)M$ and can actually be understood from the observation that the term that breaks the integrability in Eq. (21) would also be enhanced by a and η. In addition, we note that for some cases, such as the $1/2$ resonance in Fig. 3(a) and $2/3$ resonance in Fig. 5(a), the Birkhoff islands appear near the boundary of CZV. Especially, the leftmost boundary of CZV and some Birkhoff islands could be close to the (would-be) event horizons. By tuning E, L_z, and a, the closed CZV may turn into the throatlike one as shown in Fig. 1(b). This can lead to the formation/destruction of the would-be islands by the retreat/intrusion of the event horizon. We indeed do find such cases, which show the interesting effect of the event horizon on the possibility of forming/destroying the resonant islands.

In any case, our results suggest that the chaotic behaviors of the system would be enhanced by a and η and could be too small to measure when these parameters are small or even moderate. A possible implication of these results is that the attempt to detect chaotic signatures of binary systems through the gravitational waves emitted by compact binary coalescence (CBC) of comparable masses or extreme-mass-ratio inspiral (EMRI) and intermediate-mass-ratio inspiral (IMRI) would be extremely difficult. Of course, whether this is a no-go, i.e., whether the islands can generate observable signatures in gravitational waves, also depends on the dynamical timescale of the system, the population of the events, and the resolution power of the detector. Typically, the dynamical timescale of systems with tiny η such as EMRIs and IMRIs is much longer than that of CBC with sizable η, so that the passage through islands is detectable, even though the islands are very thin. However, in these cases, $a_{\rm cri}$ is in the ultraspinning regime, for which the events are rare. On the other hand, for the CBC of comparable masses, the dynamical timescale is too short to resolve the chaotic signature in the observational data unless for the detectors of high resolution. Because of the implication of our results, it requires detailed study to estimate the chance of detecting chaotic signatures in the gravitational waves of real events. We will come back to this interesting issue elsewhere.

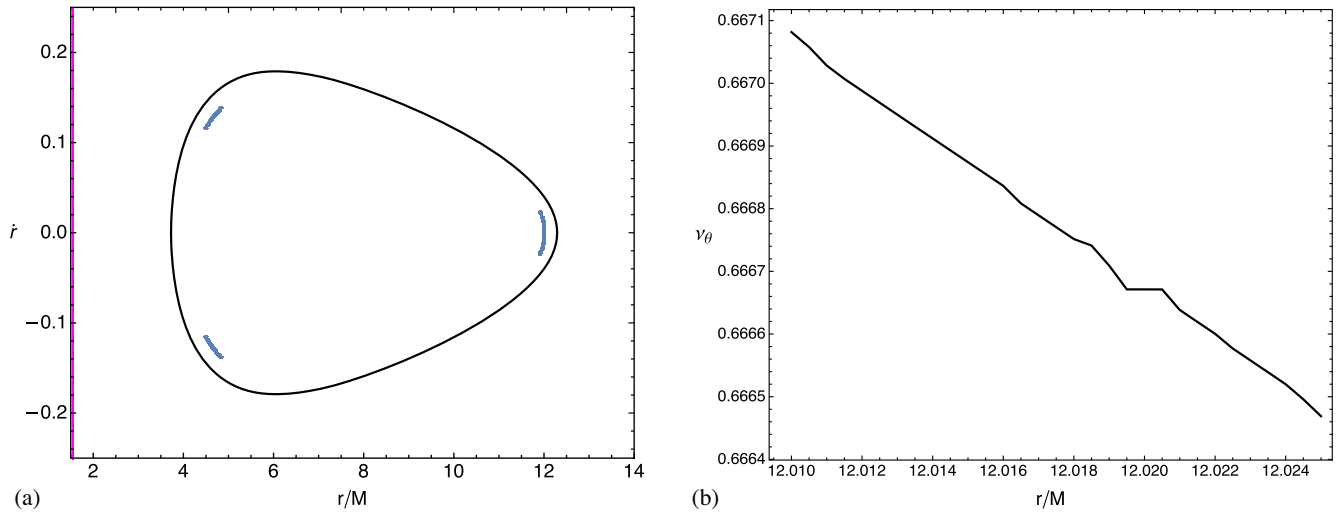

FIG. 11. (a) The $2/3$ Birkhoff islands for the 3PN effective metric for $a = 0.78\ M$ and $\eta = 0.01$. The initial conditions for the islands are $E = 0.942$, $L_z = 2.87\ M$, and $(r_0, y_0, \dot{r}_0) = (12.02M, 0, 0)$. The magenta line indicates the event horizon. (b) The rotation curve drawn along a horizontal line that crosses the rightmost branch of the islands. The plateau with $\nu_\theta = 2/3$ can be identified.

C. Some preliminary 3PN results

In this subsection, we investigate the integrability of the effective metric of EOB at 3PN order by examining the phase orbits on Poincaré surfaces of section. At 3PN order, two more terms are added into functions $F(r)$ and $G(r)$ written for up to 2PN in (19). We denote these 3PN-order functions as $F_{\rm 3PN}(r)$ and $G_{\rm 3PN}(r)$,

$$F_{\rm 3PN}(r) = \frac{2M^3}{r} + \frac{M^4}{r^2}\left(\frac{94}{3} - \frac{41}{32}\pi^2\right),$$
$$G_{\rm 3PN}(r) = \frac{1}{\eta}\ln\left[1 + 6\eta\frac{M^2}{r^2} + 2(26 - 3\eta)\eta\frac{M^3}{r^3}\right]. \quad (28)$$

The remaining structure of the effective metric at 3PN is same as the one given in (16). In EOB formulation, at 3PN, the effective Hamiltonian is not the simple freely moving particle's Hamiltonian like the one written in (9). Especially, there is an extra term, quadratic in momenta, in the square root in $H_{\rm eff}$ of (9) [5,6]. As a preliminary study, we ignore this extra term and continue with the same effective Hamiltonian as in (9) but with 3PN order $F_{\rm 3PN}$ and $G_{\rm 3PN}$ in the effective metric.

We investigate the phase orbits on the Poincaré surface of section for the 3PN case with $E = 0.942$, $L_z = 2.87\ M$, $a = 0.78\ M$, and $\eta = 0.01$ and show the results in Fig. 11. In this case, the EOB metric has a horizon, which is shown by the magenta line in Fig. 11(a). We find the $2/3$-resonant islands (blue), even when the symmetric mass ratio is small ($\eta = 0.01$). The rotation curve drawn along a horizontal line that crosses the right branch of the islands is shown in Fig. 11(b). The plateau with $\nu_\theta = 2/3$ can be clearly identified. According to these preliminary results, this "partial" 3PN dynamics may also be chaotic. In addition, the 3PN corrections seem to allow us to find Birkhoff islands even when η is small.

V. CONCLUSION

The inspiral dynamics of the compact binary black holes is intrinsically nonlinear and nonintegrable due to the nonlinearity of general relativity, which manifests as the higher orders of post-Newtonian corrections. Thus, it is very interesting to study the possibility of detecting such nonintegrability and the associated chaotic behaviors through astronomical observations, such as gravitational wave detection. If such chaotic signatures exist, one will expect to detect them in the future with more advanced technology.

In this work, we consider the effective-one-body formulation of the inspiral dynamics and study the phase orbits to find the Birkhoff chains of islands, which encode the chaotic signatures. The advantage of the EOB formulation over the usual binary dynamics is the reduction of the dynamical variables into the ones of the test body moving in a blackholelike effective metric. The reduction holds whenever the EOB dynamics is a good approximation to the original binary dynamics. This makes it easier for the formal check of the nonintegrability and the numerical study of the chaotic behavior. As a preliminary study, we consider EOB dynamics up to 2PN order and some partial 3PN-order terms. This is the lowest PN order for inspiral dynamics to be nonintegrable. For simplicity, we also turn off the spin of the test body. As expected, our results show the clear signatures of nonintegrability in the form of the Birkhoff islands. Moreover, we also show that the chaotic behaviors would be enhanced when the spin parameter a and the symmetric mass ratio η increase. This yields some implications for the issue of detecting chaos in the real gravitational wave events.

In summary, this work provides a new methodology to study the chaotic behaviors of inspiral dynamics of binary compact objects and exhibits the possible chaotic signatures. It is worthy to extend our method to higher PN EOB dynamics and include spin of the test body to obtain a more complete picture of the chaos in such dynamical systems and examine more closely the issue of their detectability.

ACKNOWLEDGMENTS

The authors thank Georgios Lukes-Gerakopoulos, Alejandro Cárdenas-Avendaño, Hsu-Wen Chiang, and Kyriakos Destounis for the fruitful suggestions on the technical parts of this work. F. L. L. is supported by Taiwan's Ministry of Science and Technology (MoST) through Grant No. 109-2112-M-003-007-MY3. A. P. is supported by MoST Grant No. 110-2811-M-003-507-MY2.

APPENDIX: SUMMARY OF DERIVING EOB MAPPING AND COMMENT ON THE INTEGRABILITY

In this appendix, we would like to summarize the procedure of constructing the EOB mapping given in [4–6] and also take the chance to comment on the integrability of the seemingly equivalent PN dynamics such as the one given in [23].

Following [4], the authors of [5,6] gave a clear procedure to construct the EOB Hamiltonian for the dynamics of binary spinning black holes. They can be summarized as follows:

(i) Start with a PN-expanded Arnowitt-Deser-Misner (ADM) Hamiltonian and then perform a canonical transformation (Lie method) to a PN-expanded Hamiltonian in EOB coordinates.
(ii) Use the results of (i) to compute the corresponding PN-expanded EOB Hamiltonian.
(iii) PN-expand the deformed Kerr Hamiltonian for a spinning test particle.
(iv) Compare (ii) and (iii) to obtain the mapping between the spin variables in the real and effective descriptions.

In general, the effective Hamiltonian of the EOB dynamics should formally be

$$H_{\rm eff} = H^{NS} + H^{S}, \tag{A1}$$

where NS denotes the part that does not involve spin of the test particle $\mathbf{S}^*$, and S is the part that involves $\mathbf{S}^*$. The PN-expanded form of $H^{NS} = \beta^i p_i + \alpha\sqrt{m^2 + \gamma^{ij} p_i p_j + Q_A(p)}$ can be summarized as follows[3]:

$$H^{NS} = H^{NS}_{S=0} + H^{NS}_{SO,1.5\rm PN} + H^{NS}_{SS,2\rm PN}. \tag{A2}$$

Here $H^{NS}_{S=0}$ is the PN Hamiltonian for the nonspinning binary, and the last two terms involve only the spin of the deformed Kerr denoted by $\mathbf{S}_{\rm Kerr}$, which is different from the spin of the test particle denoted by $\mathbf{S}^*$. The $H^{NS}_{SO,1.5\rm PN}$ is the 1.5PN spin-orbital interaction that is linear in $\mathbf{S}_{\rm Kerr}$, and $H^{NS}_{SS,2PN}$ contains the spin-spin interactions that are quadratic in $\mathbf{S}_{\rm Kerr}$. Note that H^{NS} is controlled by two metric functions $A(r)$ and $D(r)$, which are the same as the ones for the nonspinning binary up to 3PN. The terms involving $\mathbf{S}_{\rm Kerr}$ come from the Kerr terms and the additional $\tilde{\omega}_{fd}$, all of which vanish if $\mathbf{S}_{\rm Kerr}$ is set to zero.

On the other hand, H^S mainly contains terms that involve $\mathbf{S}^*$, so it vanishes if $\mathbf{S}^*$ is set to zero. The PN-expanded form of H^S can be summarized as follows:

$$H^S = H^S_{SO,1.5\rm PN} + H^S_{SO,2.5\rm PN} + H^S_{SS,2\rm PN}. \tag{A3}$$

The $H^S_{SO,1.5\rm PN}$ is the 1.5PN spin-orbital interaction that is linear in $\mathbf{S}^*$. The $H^S_{SO,2.5\rm PN}$ is the 2.5PN spin-orbital interactions linear in $\mathbf{S}^*$ but also involved $\mathbf{S}_{\rm Kerr}$. The last term $H^S_{SS,2\rm PN}$ is the spin-spin interaction and is quadratic in $\mathbf{S}^*$. This term is put in by hand, since the Hamiltonian of the test particle is valid only at the linear order of $\mathbf{S}^*$.

Step (iv) is to obtain the map below between $\mathbf{S}_{\rm Kerr}$, $\mathbf{S}^*$ of the EOB effective Hamiltonian, and $\mathbf{S}_1$ and $\mathbf{S}_2$ of the ADM Hamiltonian. Instead of using $\mathbf{S}_1$ and $\mathbf{S}_2$, one introduces

$$\boldsymbol{\sigma} = \mathbf{S}_1 + \mathbf{S}_2, \qquad \boldsymbol{\sigma}^* = \mathbf{S}_1 \frac{m_2}{m_1} + \mathbf{S}_2 \frac{m_1}{m_2}. \tag{A4}$$

The map obtained in (iv) is the following:

$$\mathbf{S}_{\rm Kerr} = \boldsymbol{\sigma} + \frac{1}{c^2}\boldsymbol{\Delta}_\sigma, \qquad \mathbf{S}^* = \boldsymbol{\sigma}^* + \frac{1}{c^2}\boldsymbol{\Delta}_{\sigma^*}, \tag{A5}$$

where

$$\boldsymbol{\Delta}_\sigma = -\frac{1}{16}\left\{12\boldsymbol{\Delta}_{\sigma^*} + \eta\left[\frac{2M}{r}(4\boldsymbol{\sigma} - 7\boldsymbol{\sigma}^*) + 6(\hat{\mathbf{p}}\cdot\hat{\mathbf{n}})^2(6\boldsymbol{\sigma} + 5\boldsymbol{\sigma}^*) - \hat{p}^2(3\boldsymbol{\sigma} + 4\boldsymbol{\sigma}^*)\right]\right\}, \tag{A6}$$

but $\boldsymbol{\Delta}_{\sigma^*}$ is an arbitrary function going to zero, at least linearly in η when $\eta \to 0$, to get the correct test particle limit. Here $\hat{\mathbf{n}} = \mathbf{r}/r$ and $\hat{\mathbf{p}} = \mathbf{p}/m$. In [5], they chose $\boldsymbol{\Delta}_{\sigma^*}$ so that $\boldsymbol{\Delta}_\sigma = 0$. In contrast, for our purpose in this work, we choose $\boldsymbol{\Delta}_{\sigma^*} = -c^2\boldsymbol{\sigma}^*$ so that $\mathbf{S}^* = 0$. Since $|\mathbf{S}_1|$, $|\mathbf{S}_2|$ and $\mathbf{L} + \mathbf{S}_1 + \mathbf{S}_2$ are conserved but not $\boldsymbol{\sigma}$ or $\boldsymbol{\sigma}^*$, thus, both the choice of [5] and ours are dynamical constraints. Furthermore, in [6] a new EOB frame is adopted so that the EOB spins $\mathbf{S}_{\rm Kerr} = \boldsymbol{\sigma}$ and $\mathbf{S}^*$ are independent of dynamical variables other than $\mathbf{S}_{1,2}$. This new EOB frame is related to the above one by a canonical transformation and a redefinition of the Hamilton-Jacobi function, and the corresponding EOB effective Hamiltonians differ at 3PN order. Again, in this new frame, we can choose to set $\mathbf{S}^*$ to zero as a dynamical constraint.

Finally, we comment on the integrable example considered in [23] and compare with the above EOB case. The ADM Hamiltonian adopted in [23] is formally the following:

$$H_{\rm Gopa} = H^{NS}_{S=0,3\rm PN} + H^S_{SO}, \tag{A7}$$

where $H^{NS}_{S=0,3\rm PN}$ is the 3PN Hamiltonian of nonspinning binary, which should correspond to EOB effective Hamiltonian of a deformed Schwarzschild background, and H^S_{SO} is the spin-orbital Hamiltonian linear in the following effective spin:

$$\mathbf{S}_{\rm eff} = g_1\mathbf{S}_1 + g_2\mathbf{S}_2, \tag{A8}$$

where the gyromagnetic factors are

$$g_1 = 2\eta\left(1 + \frac{3m_2}{4m_1}\right), \tag{A9}$$

$$g_2 = 2\eta\left(1 + \frac{3m_1}{4m_2}\right). \tag{A10}$$

The authors of [23] found integrable solutions for two special cases: (1) $m_1 = m_2$ and (2) either $\mathbf{S}_1$ or $\mathbf{S}_2$ vanishes. The Hamiltonian used in [23] differs from the ADM Hamiltonian adopted in [5,6] where gyromagnetic factors g_i of the latter involve dynamical variables $\hat{\boldsymbol{p}}'^2$, $\hat{\boldsymbol{p}}'\cdot\hat{\boldsymbol{n}}'$, and

[3] $Q_A(p)$ contains the nongeometric terms starting from 3PN order. Therefore, there is no such term in the 2PN order considered in Secs. II and IV B, and in the preliminary study of the 3PN order in Sec. IV C this term is neglected for simplicity.

M/r, in addition to the symmetric mass ratio η and the mass ratio m_1/m_2. Note that the prime is used to remind the reader that the corresponding quantity is associated with the ADM coordinate, to distinguish from those in the nonprime EOB coordinate. Also, in [5,6] they also include the 2PN spin-spin Hamiltonian

$$H_{SS}^{\mathrm{ADM}} = \frac{1}{c^4}\frac{\eta}{2r^3}[3(\hat{\boldsymbol{n}}' \cdot \boldsymbol{\sigma}_0)^2 - \boldsymbol{\sigma}_0^2], \tag{A11}$$

with $\boldsymbol{\sigma}_0 = \boldsymbol{\sigma} + \boldsymbol{\sigma}_*$. This term could be responsible for the quadratic terms of $\mathbf{S}_{\mathrm{Kerr}}$. Thus, even if we do not work out the EOB Hamiltonian from H_{Gopa} of (A7) by canonical transformation, we know that the resultant EOB effective Hamiltonian will be different from the one obtained in [5,6]. Thus, the integrable solutions in [23] are not in contradiction to the nonintegrability and chaotic features found in this work because the adopted ADM Hamiltonians are different.

[1] LIGO Scientific, VIRGO, and KAGRA Collaborations, GWTC-3: Compact binary coalescences observed by LIGO and Virgo during the second part of the third observing run, arXiv:2111.03606.

[2] A. Buonanno and T. Damour, Effective one-body approach to general relativistic two-body dynamics, Phys. Rev. D **59**, 084006 (1999).

[3] T. Damour, P. Jaranowski, and G. Schaefer, On the determination of the last stable orbit for circular general relativistic binaries at the third post-Newtonian approximation, Phys. Rev. D **62**, 084011 (2000).

[4] T. Damour, Coalescence of two spinning black holes: An effective one-body approach, Phys. Rev. D **64**, 124013 (2001).

[5] E. Barausse and A. Buonanno, An improved effective-one-body Hamiltonian for spinning black-hole binaries, Phys. Rev. D **81**, 084024 (2010).

[6] E. Barausse and A. Buonanno, Extending the effective-one-body Hamiltonian of black-hole binaries to include next-to-next-to-leading spin-orbit couplings, Phys. Rev. D **84**, 104027 (2011).

[7] N. J. Cornish, Chaos and gravitational waves, Phys. Rev. D **64**, 084011 (2001).

[8] J. J. Levin, Gravity Waves, Chaos, and Spinning Compact Binaries, Phys. Rev. Lett. **84**, 3515 (2000).

[9] J. J. Levin, The fate of chaotic binaries, Phys. Rev. D **67**, 044013 (2003).

[10] S. A. Hughes, Comment on "Gravity Waves, Chaos, and Spinning Compact Binaries," Phys. Rev. Lett. **85**, 5480 (2000).

[11] N. J. Cornish and J. J. Levin, Lyapunov timescales and black hole binaries, Classical Quantum Gravity **20**, 1649 (2003).

[12] J. D. Schnittman and F. A. Rasio, Ruling out Chaos in Compact Binary Systems, Phys. Rev. Lett. **87**, 121101 (2001).

[13] N. J. Cornish and J. J. Levin, Comment on "Ruling out Chaos in Compact Binary Systems," Phys. Rev. Lett. **89**, 179001 (2002).

[14] M. D. Hartl and A. Buonanno, The dynamics of precessing binary black holes using the post-Newtonian approximation, Phys. Rev. D **71**, 024027 (2005).

[15] X. Wu and Y. Xie, Revisit on "Ruling out chaos in compact binary systems," Phys. Rev. D **76**, 124004 (2007).

[16] X. Wu and Y. Xie, Symplectic structure of post-Newtonian Hamiltonian for spinning compact binaries, Phys. Rev. D **81**, 084045 (2010).

[17] X. Wu and S.-Y. Zhong, Regular dynamics of canonical post-Newtonian Hamiltonian for spinning compact binaries with next-to-leading order spin-orbit interactions, Gen. Relativ. Gravit. **43**, 2185 (2011).

[18] G. Cho and H. M. Lee, Analytic Keplerian-type parametrization for general spinning compact binaries with leading order spin-orbit interactions, Phys. Rev. D **100**, 044046 (2019).

[19] S. Tanay, L. C. Stein, and J. T. Gálvez Ghersi, Integrability of eccentric, spinning black hole binaries up to second post-Newtonian order, Phys. Rev. D **103**, 064066 (2021).

[20] S. Tanay, G. Cho, and L. C. Stein, Action-angle variables of a binary black-hole with arbitrary eccentricity, spins, and masses at 1.5 post-Newtonian order, arXiv:2110.15351.

[21] G. Morrás, J. García-Bellido, and S. Nesseris, Search for black hole hyperbolic encounters with gravitational wave detectors, Phys. Dark Universe **35**, 100932 (2022).

[22] A. Gopakumar and C. Konigsdorffer, The deterministic nature of conservative post-Newtonian accurate dynamics of compact binaries with leading order spin-orbit interaction, Phys. Rev. D **72**, 121501 (2005).

[23] C. Konigsdorffer and A. Gopakumar, Post-Newtonian accurate parametric solution to the dynamics of spinning compact binaries in eccentric orbits: The leading order spin-orbit interaction, Phys. Rev. D **71**, 024039 (2005).

[24] G. Huang, X. Ni, and X. Wu, Chaos in two black holes with next-to-leading order spin-spin interactions, Eur. Phys. J. C **74**, 3012 (2014).

[25] X. Wu and G. Huang, Ruling out chaos in comparable mass compact binary systems with one body spinning, Mon. Not. R. Astron. Soc. **452**, 3167 (2015).

[26] L. Huang and X. Wu, Second post-Newtonian Lagrangian dynamics of spinning compact binaries, Eur. Phys. J. C **76**, 488 (2016).

[27] V. Arnold, *Mathematical Methods of Classical Mechanics* (Springer, New York, 1989), Vol. 60.

[28] V. Frolov, P. Krtous, and D. Kubiznak, Black holes, hidden symmetries, and complete integrability, Living Rev. Relativity **20**, 6 (2017).

[29] G. O. Papadopoulos and K. D. Kokkotas, Preserving Kerr symmetries in deformed spacetimes, Classical Quantum Gravity **35**, 185014 (2018).
[30] G. Compère and A. Druart, Complete set of quasi-conserved quantities for spinning particles around Kerr, SciPost Phys. **12**, 012 (2022).
[31] G. Contopoulos, *Order and Chaos in Dynamical Astronomy* (Springer, Berlin, Heidelberg, 2002).
[32] G. Lukes-Gerakopoulos, M. Katsanikas, P. A. Patsis, and J. Seyrich, The dynamics of a spinning particle in a linear in spin Hamiltonian approximation, Phys. Rev. D **94**, 024024 (2016).
[33] E. Harms, G. Lukes-Gerakopoulos, S. Bernuzzi, and A. Nagar, Spinning test body orbiting around a Schwarzschild black hole: Circular dynamics and gravitational-wave fluxes, Phys. Rev. D **94**, 104010 (2016).
[34] G. Lukes-Gerakopoulos, Spinning particles moving around black holes: Integrability and chaos, in *Proceedings of the 14th Marcel Grossmann Meeting on Recent Developments in Theoretical and Experimental General Relativity, Astrophysics, and Relativistic Field Theories* (2017), Vol. 2, pp. 1960–1965.
[35] G. Lukes-Gerakopoulos, E. Harms, S. Bernuzzi, and A. Nagar, Spinning test-body orbiting around a Kerr black hole: Circular dynamics and gravitational-wave fluxes, Phys. Rev. D **96**, 064051 (2017).
[36] O. Zelenka, G. Lukes-Gerakopoulos, V. Witzany, and O. Kopáček, Growth of resonances and chaos for a spinning test particle in the Schwarzschild background, Phys. Rev. D **101**, 024037 (2020).
[37] V. Skoupý and G. Lukes-Gerakopoulos, Spinning test body orbiting around a Kerr black hole: Eccentric equatorial orbits and their asymptotic gravitational-wave fluxes, Phys. Rev. D **103**, 104045 (2021).
[38] I. Timogiannis, G. Lukes-Gerakopoulos, and T. A. Apostolatos, Spinning test body orbiting around a Schwarzschild black hole: Comparing spin supplementary conditions for circular equatorial orbits, Phys. Rev. D **104**, 024042 (2021).
[39] V. Skoupý and G. Lukes-Gerakopoulos, Adiabatic equatorial inspirals of a spinning body into a Kerr black hole, Phys. Rev. D **105**, 084033 (2022).
[40] I. Timogiannis, G. Lukes-Gerakopoulos, and T. A. Apostolatos, Spinning test body orbiting around a Kerr black hole: Comparing spin supplementary conditions for circular equatorial orbits, Phys. Rev. D **106**, 044039 (2022).
[41] S. Suzuki and K.-i. Maeda, Chaos in Schwarzschild spacetime: The motion of a spinning particle, Phys. Rev. D **55**, 4848 (1997).
[42] M. D. Hartl, Dynamics of spinning test particles in Kerr space-time, Phys. Rev. D **67**, 024005 (2003).
[43] M. D. Hartl, A survey of spinning test particle orbits in Kerr space-time, Phys. Rev. D **67**, 104023 (2003).
[44] K. Kiuchi and K.-i. Maeda, Gravitational waves from chaotic dynamical system, Phys. Rev. D **70**, 064036 (2004).
[45] J. R. Gair, C. Li, and I. Mandel, Observable properties of orbits in exact bumpy spacetimes, Phys. Rev. D **77**, 024035 (2008).
[46] W. Han, Chaos and dynamics of spinning particles in Kerr spacetime, Gen. Relativ. Gravit. **40**, 1831 (2008).
[47] E. E. Flanagan and T. Hinderer, Transient Resonances in the Inspirals of Point Particles into Black Holes, Phys. Rev. Lett. **109**, 071102 (2012).
[48] T. A. Apostolatos, G. Lukes-Gerakopoulos, and G. Contopoulos, How to Observe a Non-Kerr Spacetime Using Gravitational Waves, Phys. Rev. Lett. **103**, 111101 (2009).
[49] G. Lukes-Gerakopoulos, T. A. Apostolatos, and G. Contopoulos, Observable signature of a background deviating from the Kerr metric, Phys. Rev. D **81**, 124005 (2010).
[50] G. Contopoulos, G. Lukes-Gerakopoulos, and T. A. Apostolatos, Orbits in a non-Kerr dynamical system, Int. J. Bifurcation Chaos Appl. Sci. Eng. **21**, 2261 (2011).
[51] J. Brink, M. Geyer, and T. Hinderer, Orbital Resonances around Black holes, Phys. Rev. Lett. **114**, 081102 (2015).
[52] J. Brink, M. Geyer, and T. Hinderer, Astrophysics of resonant orbits in the Kerr metric, Phys. Rev. D **91**, 083001 (2015).
[53] A. Cárdenas-Avendaño, A. F. Gutierrez, L. A. Pachón, and N. Yunes, The exact dynamical Chern–Simons metric for a spinning black hole possesses a fourth constant of motion: A dynamical-systems-based conjecture, Classical Quantum Gravity **35**, 165010 (2018).
[54] K. Destounis, A. G. Suvorov, and K. D. Kokkotas, Testing spacetime symmetry through gravitational waves from extreme-mass-ratio inspirals, Phys. Rev. D **102**, 064041 (2020).
[55] G. Lukes-Gerakopoulos and V. Witzany, Non-linear effects in EMRI dynamics and their imprints on gravitational waves, arXiv:2103.06724.
[56] K. Destounis, A. G. Suvorov, and K. D. Kokkotas, Gravitational-Wave Glitches in Chaotic Extreme-Mass-Ratio Inspirals, Phys. Rev. Lett. **126**, 141102 (2021).
[57] G. Lukes-Gerakopoulos, The non-integrability of the Zipoy-Voorhees metric, Phys. Rev. D **86**, 044013 (2012).
[58] O. Zelenka and G. Lukes-Gerakopoulos, Chaotic motion in the Johannsen-Psaltis spacetime, in *Proceedings of the Workshop on Black Holes and Neutron Stars* (2017), arXiv:1711.02442.
[59] G. Lukes-Gerakopoulos and O. Kopáček, Recurrence analysis as a tool to study chaotic dynamics of extreme mass ratio inspiral in signal with noise, Int. J. Mod. Phys. D **27**, 1850010 (2017).
[60] K. Destounis and K. D. Kokkotas, Gravitational-wave glitches: Resonant islands and frequency jumps in non-integrable extreme-mass-ratio inspirals, Phys. Rev. D **104**, 064023 (2021).
[61] S. Mukherjee, O. Kopacek, and G. Lukes-Gerakopoulos, Resonance crossing of a charged body in a magnetized Kerr background: An analogue of extreme mass ratio inspiral, arXiv:2206.10302.
[62] H. G. Schuster and W. Just, *Deterministic Chaos: An Introduction* (Wiley-VCH, New York, 2005).
[63] E. Barausse, E. Racine, and A. Buonanno, Hamiltonian of a spinning test-particle in curved spacetime, Phys. Rev. D **80**, 104025 (2009).
[64] J. Steinhoff, Spin gauge symmetry in the action principle for classical relativistic particles, arXiv:1501.04951.
[65] G. Faye, L. Blanchet, and A. Buonanno, Higher-order spin effects in the dynamics of compact binaries. I. Equations of motion, Phys. Rev. D **74**, 104033 (2006).

[66] C. Zhang, W.-B. Han, and S.-C. Yang, Analytical effective one-body formalism for extreme-mass-ratio inspirals with eccentric orbits, Commun. Theor. Phys. **73**, 085401 (2021).

[67] C. Zhang, W.-B. Han, X.-Y. Zhong, and G. Wang, Geometrized effective-one-body formalism for extreme-mass-ratio limits: Generic orbits, Phys. Rev. D **104**, 024050 (2021).

[68] S. Benenti and M. Francaviglia, Remarks on certain separability structures and their applications to general relativity, Gen. Relativ. Gravit. **10**, 79 (1979).

[69] Z. Cao and W.-B. Han, Waveform model for an eccentric binary black hole based on the effective-one-body-numerical-relativity formalism, Phys. Rev. D **96**, 044028 (2017).

[70] C. Verhaaren and E. W. Hirschmann, Chaotic orbits for spinning particles in Schwarzschild spacetime, Phys. Rev. D **81**, 124034 (2010).

[71] A. J. Lichtenberg and M. A. Lieberman, *Regular and Chaotic Dynamics* (Springer, New York, 1992).

[72] N. Voglis and C. Efthymiopoulos, Angular dynamical spectra. A new method for determining frequencies, weak chaos and cantori, J. Phys. A **31**, 2913 (1998).